Proceedings in Manufacturing Systems, Volume 20, Issue 4, 2025, pp. 161-174 ISSN 2067-9238

NUMERICAL ASSESSMENT OF THE STRUCTURAL INTEGRITY OF UAV SHAFTS RECONDITIONED BY THERMAL SPRAYING

Sorin-Constantin BOTEZ[1,*], Corina BOTEZ[2], George CONSTANTIN[3]

[1, 2)] Lecturer, PhD, Graphics Engineering and Industrial Design Department, POLITEHNICA Bucharest, Romania
[3)] Prof., PhD, Robots and Manufacturing Systems Department, POLITEHNICA Bucharest, Romania

Abstract: *The present study investigates the structural behavior of unmanned aerial vehicle (UAV) shafts reconditioned through thermal spray coatings, with emphasis on stress distribution and integrity under operational loading conditions. UAV shaft components are subjected to combined axial, torsional, and bending loads, leading to progressive surface degradation and potential failure in critical regions. Thermal spraying represents an efficient reconditioning technique; however, the addition of a coating layer alters the mechanical response of the component, particularly at geometric discontinuities. A three-dimensional finite element model was developed to simulate the mechanical response of coated shafts, incorporating both substrate and coating material properties. The analysis considers realistic service loads and focuses on key geometric parameters, including shaft diameter, fillet radius, and coating thickness. A simulation plane of nine tests was employed to evaluate the influence of these parameters on stress distribution in critical regions, namely the frontal area, cylindrical section, and fillet zone. The results demonstrate that the fillet radius is the most influential parameter governing stress concentration, while coating thickness significantly affects stress redistribution, especially at the coating–substrate interface. Higher stiffness coatings tend to shift stress concentrations toward the interface, whereas lower stiffness coatings exhibit elevated stress levels within the coating layer. Although no statistically significant effects were identified due to limited dataset size, consistent trends indicate the dominant role of geometric parameters in controlling stress behavior. The findings provide valuable guidelines for the design and optimization of reconditioned UAV shafts, highlighting the necessity of balancing coating thickness and geometric features to minimize stress concentrations and ensure structural reliability.*

Key words: *UAV shafts, thermal spraying, finite element analysis, structural integrity, stress concentration, coating thickness, fillet radius*.

1. INTRODUCTION

Unmanned Aerial Vehicles (UAVs) are increasingly employed in civil, industrial, and defense applications, where reliability, lightweight design, and cost-effective maintenance are critical requirements. Among the mechanical components of UAV propulsion and transmission systems, rotating shafts supporting rolling bearings are particularly susceptible to surface degradation phenomena such as wear, fretting, and localized plastic deformation. These damage mechanisms can compromise dimensional accuracy and structural integrity, ultimately leading to premature failure.

In aerospace and UAV applications, the replacement of damaged shafts is often associated with high costs and extended downtime. As a result, reconditioning technologies have gained considerable attention as sustainable alternatives to component replacement. Thermal spraying is widely used for the repair of cylindrical components due to its ability to restore dimensions, improve surface properties, and apply a wide range of functional coatings with minimal thermal impact on the substrate.

Thermal spray processes such as High-Velocity Oxygen Fuel (HVOF) and Atmospheric Plasma Spraying (APS) are commonly employed for shaft repair in aerospace and industrial sectors. These techniques allow the deposition of dense coatings with high adhesion strength, making them suitable for load-bearing applications. However, the introduction of a coating layer alters the local stiffness, stress distribution, and load transfer mechanisms within the component, particularly in geometrically critical regions such as bearing shoulders and fillets.

Despite the widespread industrial use of thermal spraying for shaft reconditioning, the structural integrity of reconditioned components is often assessed empirically, relying on experience-based criteria or simplified strength checks. Experimental investigations are costly and may not capture the complex stress states arising from the interaction between coating, substrate, and operational loads. In this context, Finite Element Method (FEM) simulations represent an effective tool for evaluating the mechanical behavior of reconditioned components under realistic loading conditions.

Previous numerical studies on thermally sprayed components have primarily focused on residual stress

[*] Corresponding author: Splaiul Independenței 313, district 6, 060042, Bucharest, Romania,
Tel.: 0040 21 402 9420
E-mail address: *botez.sorin.constantin@gmail.com* (S.-C. Botez)

development, coating adhesion, or simplified geometries. However, detailed FEM investigations addressing load-bearing UAV shafts with bearing shoulders remain limited, particularly regarding the influence of the reconditioning layer on stress concentration zones critical for structural integrity.

The objective of the present study is to provide a numerical assessment of the structural integrity of a UAV shaft reconditioned by thermal spraying, using finite element analysis. A detailed three-dimensional model of a cylindrical shaft with a bearing shoulder is developed, incorporating both substrate and coating materials. The stress distribution, critical regions, and the influence of coating thickness are analyzed and compared with the unreconditioned configuration. The results aim to support engineering decision-making regarding the feasibility and safety of thermal spray reconditioning for UAV rotating components.

2. LITERATURE REVIEW

2.1. Thermal spray processes and applications

Thermal spray technologies are widely applied in engineering to deposit functional and protective coatings on substrates to enhance wear, corrosion, and fatigue performance in mechanical systems. Common processes include high-velocity oxygen fuel (HVOF), atmospheric plasma spraying (APS), cold spray, and arc spray, each characterized by specific particle impact velocities, thermal inputs, and coating microstructures. These parameters strongly influence adhesion, porosity, mechanical properties, and residual stress states in the deposited coatings. The *Journal of Thermal Spray Technology* regularly publishes developments in coating performance and optimization across industrial sectors including aerospace and power generation [1].

The microstructure and residual stress state of thermally sprayed coatings are strongly dependent on process parameters and particle dynamics during deposition. For example, Wang et al. examined FeMnCrSi HVOF coatings and demonstrated that variations in standoff distance, fuel/oxygen ratio, and powder feed rate significantly influence particle velocity and coating residual stresses, which in turn affect wear resistance [2]. This highlights the importance of understanding process-structure-property relationships when applying coatings for functional performance or repair.

2.2. Residual stresses in thermal spray coatings

Residual stresses generated during thermal spray deposition have been identified as a key factor affecting coating integrity, adhesion and service life. These stresses originate from particle impact (“peening”) and quenching during rapid solidification, as well as thermal mismatch between the coating and substrate during cooling [3]. Early numerical investigations by Bansal *et al.* demonstrated that particle velocity and temperature significantly influence residual stress formation in HVOF coatings [4], and that such stresses can degrade adhesion and promote interfacial defects when not properly controlled.

Finite element modeling (FEM) has been used to simulate the evolution of residual stresses in thermally sprayed layers [5]. Modeling methodologies range from microstructural-based techniques using adaptive meshing to macroscopic thermo-mechanical analyses incorporating thermal mismatch strains [3] [5]. These models reveal that coating thickness, deposition intervals, and thermal gradients significantly affect residual stress distribution and can lead to tensile stress states that compromise coating performance [6]. Moreover, multi-scale thermo-mechanical simulation has been proposed to study the evolution of stress from the splat scale to the part scale, providing deeper insight into coating/substrate interactions [7].

Experimental techniques such as X-ray diffraction and curvature methods have also been employed to quantify residual stresses in sprayed coatings and validate numerical predictions [8]. These studies confirm that residual stress profiles exhibit complex gradients through the coating thickness and can transition between tensile and compressive states depending on process parameters and material combinations.

2.3. Mechanical performance and structural integrity

Thermal spray coatings influence not only wear and erosion resistance but also mechanical performance under cyclic and service loading. Residual stresses can significantly impact the initiation and growth of fatigue cracks, particularly in load-bearing components subject to multi-axial stress states. Lin et al. highlighted that the dense microstructures achieved by optimized APS and HVOF processes contribute to superior mechanical performance, partly due to favorable residual stress profiles [9]. In maritime applications, correlation studies of residual stress and coating properties demonstrated how stress influences adhesion and mechanical robustness across different substrates [10].

While these studies emphasize the critical role of residual stresses in coating behavior, most experimental and numerical work has focused on flat substrates or simplified geometries, limiting direct applicability to complex components such as shaft bearing shoulders typical of UAV applications.

2.4. Numerical modeling of spray coatings

Finite element analysis has been widely adopted to predict the stress state and performance of thermally sprayed coatings under operational conditions. Early work by researchers such as Ng and Gan developed FEM techniques to predict as-sprayed residual stresses in plasma spray coatings, demonstrating the sensitivity of stress distributions to process and material variables [11]. Subsequent studies modeled residual stress for various thermal spray processes including HVOF and plasma spray, focusing on how particle impact dynamics and substrate interaction contribute to stress evolution [4], [12] [13].

More recent research in multi-scale modeling and analysis aims to connect microstructural and macroscopic features by incorporating coupled thermo-mechanical analyses that simulate thermal gradients and stress evolution during coating deposition. [5] [7] [14] [15] [16] [17] [18] [19]. These approaches provide a

pathway to understand how residual stresses interact with part geometry – a critical consideration for reconditioned shafts with shoulders and other stress concentrations.

2.5. Knowledge gaps and relevance in UAV shaft reconditioning

Despite significant advances in thermal spray process understanding and residual stress modeling, the literature lacks comprehensive FEM studies that integrate realistic component geometries, thermal spray layering effects, and operational load cases. Specifically, there are few studies assessing the structural integrity of thermally sprayed and reconditioned load-bearing shafts with complex features such as bearing shoulders under representative mechanical loading. This gap underscores the need for detailed numerical analyses that evaluate how thermally sprayed coatings influence stress concentration regions, fatigue resistance, and functional performance in systems such as UAV drivetrains.

3. UAV SHAFT LOADS AND THEIR RELEVANCE TO THERMALLY SPRAYED RECONDITIONED SHAFTS

UAV propulsion shafts are subjected to combined axial, torsional, and bending loads generated by propeller thrust, motor torque transmission, and dynamic flight conditions. These loading components are directly relevant to the structural integrity of thermally sprayed reconditioned shafts, as they govern stress localization at the coating–substrate interface and in geometrical discontinuities such as bearing shoulders.

Electric UAV propulsion systems typically operate at rotational speeds between 3,000 and 10,000 rpm, depending on vehicle scale and propulsion architecture [20] [21].

Small multirotor UAVs commonly employ high-speed propellers operating above 5,000 rpm to generate sufficient thrust, whereas larger UAVs and VTOL systems use lower rotational speeds combined with larger propeller diameters [22].

These high rotational speeds amplify centrifugal effects and increase the sensitivity of the shaft to surface condition and material heterogeneity. In reconditioned shafts, differences in elastic modulus and density between the base material and the thermally sprayed layer may influence stress redistribution under high-speed rotation, making accurate load representation essential in FEM-based integrity assessments.

3.1. Axial loads

Propeller thrust generates a dominant axial load component acting on the shaft. Although axial stresses are often lower than torsional or bending stresses, they play a significant role in bearing life and contact pressure distribution, particularly in high-thrust or vertical take-off and landing (VTOL) UAVs.

Thermal effects and assembly preloads may also contribute to axial loading, especially in precision assemblies.

Experimental studies report thrust forces ranging from approximately 10 N to over 120 N per propeller for typical UAV configurations operating between 4,000 and 6,500 rpm [23]. Similar thrust ranges were observed in quadrotor aerodynamic modeling studies, representative for small- and medium-scale UAV shafts [24]. In the context of thermally sprayed reconditioning, these axial forces are transmitted through the coating layer toward the bearing shoulder region. Such loading conditions promote stress concentration at the coating–substrate interface, where coating adhesion strength and residual stresses play a critical role [25].

3.2. Torsional loads

The primary load acting on UAV propulsion shafts is torsion, generated by torque transmission from electric motors or internal combustion engines to propellers or rotors. The magnitude of torsional stress depends on motor power, rotational speed, and propeller aerodynamic resistance. Rapid throttle changes, common in UAV maneuvering and control, induce transient torsional loads, which may exceed steady-state values and contribute to fatigue damage.

In electric UAVs, torque ripple from brushless DC motors can further introduce cyclic torsional stresses, particularly at low rotational speeds. These effects are often critical in lightweight shafts with reduced polar moments of inertia.

The torsional loads transmitted by the shaft arise from the torque required to drive the propeller and overcome aerodynamic resistance. Analytical and experimental models indicate that torque values for UAV propulsion systems range from sub-newton-meter levels in small drones to several newton-meters in medium-size UAVs, depending on propeller diameter and operating regime [26] [27] [28]. These torsional loads are particularly critical for thermally sprayed coatings, as shear stresses develop parallel to the interface. The equivalent von Mises stress patterns observed in the reconditioned shaft model indicate that torsion significantly contributes to combined stress states within the coating and near the interface.

A well-known *empirical representation* of the Thrust force and torque used in UAV and rotorcraft aerodynamics is:

$$T = C_T \rho n^2 D^4, \tag{1}$$

$$Q = C_Q \rho n^2 D^4. \tag{2}$$

where:

T – thrust force (N),
Q – torque (N·m),
C_T – thrust coefficient (0.08–0.11),
C_Q – torque coefficient (0.01 – 0.03),
ρ – air density (at 20 °C and 101.325 kPa, $\rho = 1.2041$ kg/m^3),
n – propeller rotation speed (rev/s),
D – propeller diameter.

3.3. Bending loads

In addition to axial and torsional loading, bending moments arise due to the followings [29].

- Aerodynamic thrust forces acting on the propeller,
- Unsteady aerodynamic forces, especially during forward flight or maneuvering,

- Propeller overhang,
- Weight of the propeller and hub,
- Mass imbalance,
- Misalignment between motor shaft and propeller axis,
- Manufacturing tolerances and assembly errors.

Cantilevered shaft configurations, frequently used in small and medium UAVs, are especially sensitive to bending loads. These loads generate tensile and compressive stresses that superimpose on torsional stresses, leading to combined stress states at critical locations such as bearing shoulders and fillets.

Such bending loads introduce tensile–compressive stress cycles at the shaft surface, where thermally sprayed coatings are most susceptible to cracking and delamination. The bending-induced stress gradients identified in the present FEM analysis highlight the necessity of considering realistic UAV bending loads when evaluating the structural performance of reconditioned shafts.

3.4. Vibratory and Dynamic Loads

UAV shafts are subject to dynamic excitation due to:

- Propeller imbalance,
- Aerodynamic disturbances (gusts, turbulence),
- Motor-induced vibrations,
- Structural resonances.

These excitations can lead to high-cycle fatigue, particularly if operating speeds approach natural frequencies of the shaft–bearing–propeller system. Resonance conditions are especially critical for lightweight shafts with low damping.

3.5. Fatigue Loading

Given the repetitive nature of UAV missions, fatigue loading is a dominant design consideration. UAV shafts typically experience [30]:

- High-cycle fatigue due to steady rotational motion,
- Low-cycle fatigue due to start–stop operations and aggressive maneuvers.

Stress concentrations at geometric discontinuities – such as shoulders for bearing placement or keyways – serve as preferential crack initiation sites. Surface condition, residual stresses , and reconditioning methods (e.g., thermal spraying) significantly influence fatigue performance.

3.6. Thermal and environmental loads

Thermal loads arise from:

- Motor heat generation,
- Friction at bearings,
- Environmental temperature variations.

These loads may induce thermal expansion mismatches between shaft, coating, and bearings, altering contact pressures and stress distributions. Environmental factors such as humidity, dust, and corrosion may further degrade surface integrity and fatigue resistance.

3.7. Combined loading effects

In real operating conditions, UAV shafts are subjected to combined torsional, bending, axial, and dynamic loads. The interaction of these load components leads to multiaxial stress states that cannot be accurately assessed using simplified analytical methods alone. As a result, finite element analysis (FEA) has become a standard tool for evaluating UAV shaft integrity under realistic service conditions.

3.8. Relevance for FEM-based reconditioning studies

Understanding the nature and magnitude of UAV shaft loads is essential for evaluating the effectiveness of reconditioning techniques such as thermal spraying. Load-induced stress concentrations identified through FEM provide the basis for assessing whether reconditioned shafts can safely meet operational requirements without compromising structural integrity or fatigue life.

Overall, the literature indicates that UAV shafts operate under combined multi-axial loading, characterized by thrust forces of 10–120 N, torque levels of 0.5–8 N·m, and rotational speeds of several thousand rpm. These quantitative load ranges provide a validated basis for the boundary conditions applied in the finite element analysis of the thermally sprayed reconditioned shaft presented in this study. By directly linking realistic UAV operational loads to coating-level stress responses, the present analysis enables a more reliable assessment of the suitability of thermal spray reconditioning for UAV propulsion components.

The combined axial, torsional, and bending loads acting on UAV propulsion shafts and their influence on the reconditioned regions are summarized in Table 1. These load ranges could be directly applied as boundary conditions in the FEM model to evaluate stress localization within the thermally sprayed coating and at the coating–substrate interface.

4. CRITICAL SHAFT GEOMETRY

It is found from design experience that certain areas of shafts subjected to complex stresses are more sensitive in operation. In the case studied, the transition areas from the bearing seating surfaces to their support shoulders are the most stressed. Therefore, the study will also include the geometric parameters that define these areas.

In general, bearings are mounted on cylindrical surfaces of the shaft having a diameter with a tight fit with the inner ring of the bearing. This seat surface is connected to the flat annular shoulder having the height h surfaces by circular surfaces of radius ra (Fig. 1) [36]. Another possible situation is that with a grinding undercut used for transition from the cylindrical bearing support surface to the shoulder (Fig. 2). The solution with an intermediate ring with a bevel is not considered in this study.

The height of the shaft and housing shoulders h must exceed the maximum permissible chamfer dimension of the bearing r_a, ensuring that the bearing seats firmly against the flat face of the shoulder. This guarantees proper load transfer and correct positioning of the bearing.

At the same time, the fillet radius of the shaft r_a should be smaller than the minimum allowable chamfer dimension of the bearing r, in order to avoid interference that could prevent proper seating of the bearing:

$$r_a = (0.7\ldots0.9)\, r_{min}. \quad (3)$$

Table 1

Typical UAV shaft loads and their relevance to the FEM analysis of a thermally sprayed reconditioned shaft

Load Type	Typical Quantitative Range (Literature)	Primary Source of Load	Affected FEM Region(s)	Observed / Expected FEM Effect
Axial load (thrust)	10–120 N	Propeller aerodynamic thrust	Bearing shoulder, coating-substrate interface	Axial stress concentration at shoulder fillet; increased normal stresses at interface
Torsional load (torque)	0.5–8 N·m	Propeller aerodynamic drag and motor output	Entire shaft cross-section; coating layer	Elevated shear stresses in coating; contribution to von Mises stress near interface
Bending moment	0.1–5 N·m (equivalent)	Propeller overhang, mass imbalance, aerodynamic asymmetry	Shaft surface at coating; shoulder transition zone	Tensile–compressive stress gradients; risk of coating cracking or delamination
Rotational speed	3,000–10,000 rpm	Electric motor operation	Coating layer and near-surface substrate	Centrifugal stress amplification; sensitivity to coating material mismatch
Dynamic load fluctuations	±20–40% of nominal loads	Maneuvering, throttle transients	Coating-substrate interface	Increased fatigue damage potential; interface debonding risk

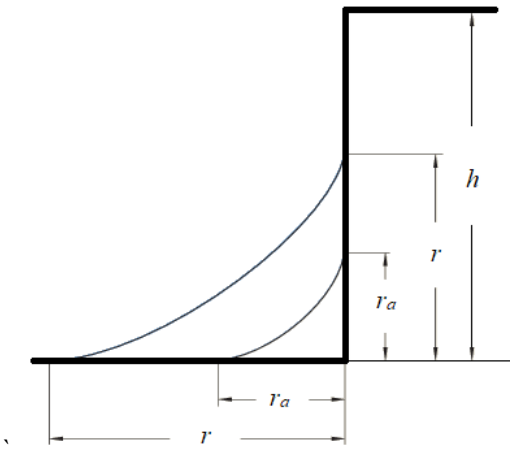

Fig. 1. Bearing mounting on shaft: *a* – fillet surface: *b* – grinding undercut; *c* – mounting with spacer.

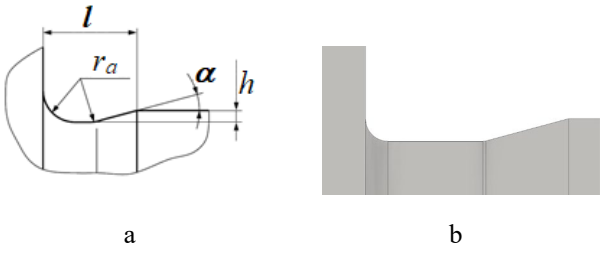

Fig. 2. Shaft model with with a grinding undercut: *a* – schematic with dimensions; *b* – 3D model.

Reference values for the shoulder height h and fillet radius r_a are provided in bearing producer catalogues [37]. In applications involving significant axial loads, it is recommended that the shoulder height be increased beyond the tabulated values to ensure adequate support.

5. MATERIAL PROPERTIES FOR THE THERMALLY SPRAYED COATINGS

Material properties for the thermally sprayed coatings were adopted from literature and are summarized in Tables 2–4. The elastic modulus of the coatings was reduced relative to bulk material values to account for porosity and splat-based microstructure typical of thermal spray processes. All materials were modeled as linear elastic and isotropic, consistent with common practice in FEM studies of thermally sprayed components.

The thermally sprayed coatings were modeled with realistic, process-informed material properties. For WC–Co cermet coatings applied by HVOF, density and elastic modulus values were taken from literature reports of low-porosity, dense microstructures typical of thermal spray processes, with Young's modulus in the 140–300 GPa range and porosity below 5 %. Al_2O_3–TiO_2 ceramic coatings, also thermally sprayed, exhibit broader elastic modulus values from ~77 GPa up to ~180 GPa depending on spray method, with higher porosity for APS variants. Thermal conductivity and coefficient of thermal expansion values were similarly selected based on measured trends for cermet versus ceramic coatings. These properties ensure that the finite element material assignments reflect the mechanical anisotropy and stiffness contrasts relevant to stress distributions in reconditioned shafts.

The materials considered are alloy steel for the shaft and bearing steel for the inner ring of the bearing. The materials have very similar properties. Therefore, for the numerical simulation, identical Young's modulus of elasticity, E = 210,000 MPa, as well as Poisson's ratio, ν = 0.3, will be considered.

6. NUMERICAL SIMULATION USING FEA

Both the substrate material and the thermally sprayed coating were assumed to exhibit linear elastic, isotropic behavior. Plastic deformation, creep, and viscoelastic effects were not considered, as the applied loads were selected to remain below the yield strength of both materials.

Typical elastic properties used for the thermally sprayed coating (e.g., steel-based or ceramic-metal composite coatings) were defined based on literature data, accounting for the reduced stiffness commonly

Table 2

Mechanical and thermal properties of HVOF-sprayed steel coatings [31] [32]
(Typical Fe-based or stainless steel coatings used for shaft repair)

Property	Symbol	Typical Value / Range	Unit	Notes
Density	ρ	7200–7800	$kg \cdot m^{-3}$	Slightly lower than bulk steel due to porosity
Young's modulus	E	140–200	GPa	Reduced vs. bulk steel (~210 GPa)
Poisson's ratio	ν	0.25–0.30	–	Commonly assumed isotropic
Yield strength (effective)	σ_γ	300–600	MPa	Depends on porosity and splat bonding
Ultimate strength	σ_u	600–900	MPa	Higher scatter than bulk material
Thermal conductivity	k	15–30	$W \cdot m^{-1} \cdot K^{-1}$	Lower than wrought steel
Coefficient of thermal expansion	α	$(10–13) \times 10^{-6}$	K^{-1}	Comparable to steel substrate

Recommended FEM use: structural reconditioning layers, load-bearing coatings, shafts and journals.

Table 3

Mechanical and thermal properties of WC–Co (HVOF-sprayed) coatings [33] [34] [35]
(Widely used for wear-resistant shaft reconditioning)

Property	Symbol	Typical Value / Range	Unit	Notes
Density	ρ	13,500–14,500	$kg \cdot m^{-3}$	Depends on Co content
Young's modulus	E	300–550	GPa	Strongly reduced vs. bulk WC (~700 GPa)
Poisson's ratio	ν	0.20–0.24	–	Common assumption
Fracture strength (effective)	σ_f	800–1500	MPa	Brittle behavior
Hardness	HV	900–1300	HV	Strong wear resistance
Thermal conductivity	k	60–90	$W \cdot m^{-1} \cdot K^{-1}$	Higher than steel
Coefficient of thermal expansion	α	$(4.5–6.5) \times 10^{-6}$	K^{-1}	Mismatch vs. steel substrate
Porosity (vol.)	–	0.5–2	%	Very dense with HVOF

Recommended FEM use: high-stress shear and contact regions; interface stresses must be checked carefully.

Table 4

Mechanical and thermal properties of Al_2O_3 thermal spray coatings [32] [34]
(APS or HVOF ceramic coatings)

Property	Symbol	Typical Value / Range	Unit	Notes
Density	ρ	3600–3900	$kg \cdot m^{-3}$	Lower than bulk alumina
Young's modulus	E	120–200	GPa	Highly dependent on porosity
Poisson's ratio	ν	0.21–0.24	–	Often assumed constant
Tensile strength (effective)	σ_t	100–300	MPa	Brittle
Compressive strength	σ_c	>1500	MPa	Very high
Thermal conductivity	k	5–15	$W \cdot m^{-1} \cdot K^{-1}$	Much lower than metals
Coefficient of thermal expansion	α	$(6.5–8.5) \times 10^{-6}$	K^{-1}	Large mismatch vs. steel
Porosity (vol.)	–	5–15	%	Typical APS range

Recommended FEM use: non-load-bearing or hybrid coatings; tensile stresses critical.

observed in sprayed materials due to porosity and splat interfaces. The elastic modulus of the coating was therefore assumed to be lower than that of the bulk substrate material, while Poisson's ratio was taken within conventional ranges reported for thermally sprayed deposits.

The interface between the thermally sprayed coating and the substrate was modeled as a perfectly bonded contact, implying full displacement continuity and no relative slip or separation under loading. This assumption corresponds to an ideal adhesion condition and represents the upper bound of structural integrity for a reconditioned shaft.

Interfacial defects, such as incomplete bonding, microcracks, or oxide layers, were not explicitly modeled. As a result, potential interfacial debonding or damage evolution was not considered in the present analysis and is deferred to future work.

The applied loads (Tabels 1 and 5) were derived from representative UAV operational conditions and included axial, torsional, and bending components. Axial loads were applied to simulate propeller thrust transmission through the shaft, while torsional moments represented the torque required to drive the propeller. Bending moments were introduced to account for propeller overhang and aerodynamic asymmetry.

Dynamic effects associated with transient maneuvers, vibration, or imbalance were not included in the current model.

The contact pressure caused by the tight fit of the bearing on the shaft is calculated as a function of interference and for a k6–m6 fit. According to design experience, these can be average values for the diameters of the seating surfaces of 12 mm, 17 mm and 25 mm:

$$\delta 12 = 0.008 \text{ mm}; \ \delta 17 = 0.010 \text{ mm}; \ \delta 25 = 0.014 \text{ mm}. \quad (4)$$

The contact pressure is calculated with the relation:

$$p = \frac{\delta}{d\left(\frac{1-\nu^2}{E} + \frac{1-\nu^2}{E}\right)} = \frac{\delta}{2d\frac{1-\nu^2}{E}} \quad (5)$$

Consideration was given to replacing the reactions in the bearings with the contact pressure between the shaft and the bearing, which will overlap the pressure caused by interference in the assembly.

Similarly, the thrust force acting on the annular surface of the shaft shoulder is replaced by the contact pressure exerted by the inner ring of the bearing on the shaft.

The thermal spraying process was not explicitly simulated. Consequently, residual stresses induced during deposition and temperature gradients generated during spraying were not included in the present model. The coating was assumed to be deposited stress-free at ambient temperature prior to mechanical loading.

This simplification allows the isolated assessment of service-induced stresses; however, it may underestimate the total stress state in the coating and at the interface. The incorporation of spray-induced residual stresses is identified as a critical topic for future investigations.

The experimental plan was established based on a Taguchi experimental plan L9 (3 × 3) that was extended to nine variable parameters (factors) considered, which are not all independent. Thus, the experimental plan takes in consideration three parameters with three levels – the inner diameter of the bearing d, connection radius r_a, and the layer material. The last five parameters depends on the shaft diameter – layer thickness s, axial contact pressure p_{ax}, shaft seat pressure $P_{cyl\text{-max}}$, thrust force T, torque Q, and shouder hight h (Table 5). Of these, the connection radius r_a has three values, but the set of values is different depending on the diameter d. The rest of parameters (p_a, $P_{cyl\text{-max}}$, T, Q and h) have a single value for each diameter considered. Table 5 presents the experimental design used for FEA, including the parameters used in the modeling, as well as the bending moment M_{bend} caused by the radial force of the propeller and the bearing reactions R_A and R_B due to this force and the weight of the shaft.

The material used in simulations are the shaft basis material – low alloyed steel (40C8, HB 220), and two materials for the layer – WC–Co HVOF-sprayed (Table 3) and Al_2O_3 (Table 4).

The shaft was modeled based on the schematic shown in Fig. 3, *a*, without thermal sprayed layer (Fig. 3,*b*), and including this layer (Fig. 4). The latter was modeled using a simplification, namely as having a constant thickness s for all surfaces (cylindrical, annular and connection surface of radius r_a or grinding undercut surface) (free moved layer, Fig. 4,*a*) and considered only for the side to propeller (Fig. 4, *b*).

The finite element mesh consisted of three-dimensional solid elements, with local refinement applied in regions of interest, including the coating layer, the coating-substrate interface, and the bearing shoulder fillet (Figs. 5 and 6). Mesh convergence was verified by monitoring stress values in critical regions to ensure solution independence from element size.

Linear static analysis was performed, and geometric nonlinearity was neglected, as deformations remained small relative to characteristic dimensions.

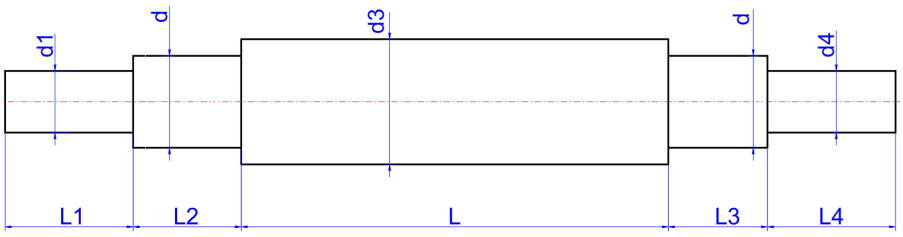

a

b

Fig. 3. Shaft model: *a* –schematic with dimensions; *b* – 3D model.

Table 5

Test plan used for shaft model numerical simulation

Test	d (mm)	r_a (mm)	Thickness s (mm)	Material	P_{ax} (MPa)	$P_{cyl\text{-}max}$ (MPa)	R_A (N)	R_B (N)	Thrust T (N)	Torque Q (Nm)	M_{bend} (Nm)	h (mm)
1	12	0.161	0.02	Steel (without layer)	0.88	77	55	46	30	1.5	5	1.5
2	12	0.184	0.05	WC–Co								
3	12	0.207	0.1	Al_2O_3								
4	17	0.32	0.1	Steel (without layer)	1.02	68	46	74	55	2.5	7	2.25
5	17	0.32	0.02	WC–Co								
6	17	0.28	0.05	Al_2O_3								
7	25	0.72	0.05	Steel (without layer)	1.31	65	62	118	100	5	15	2.75
8	25	0.56	0.1	WC–Co								
9	25	0.64	0.02	Al_2O_3								

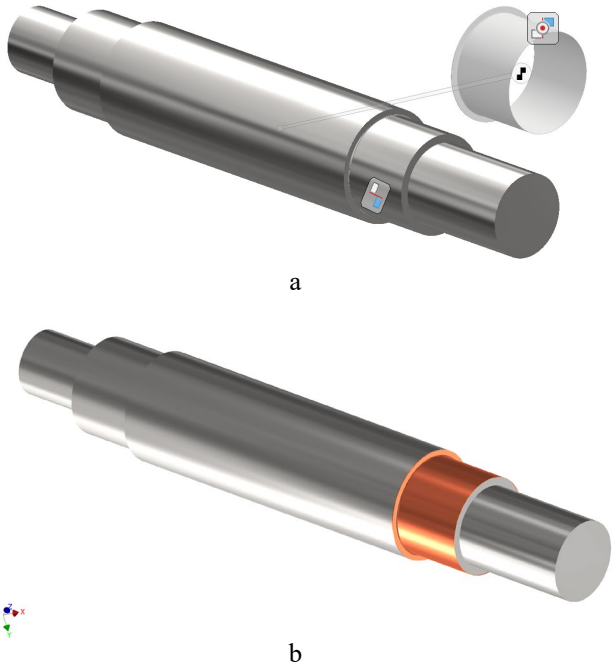

Fig. 4. Shaft model and layer models (simplification – side to propeller): *a* – shaft and free moved thermal sprayed layer; *b* – with layer on the propeller side for simplicity.

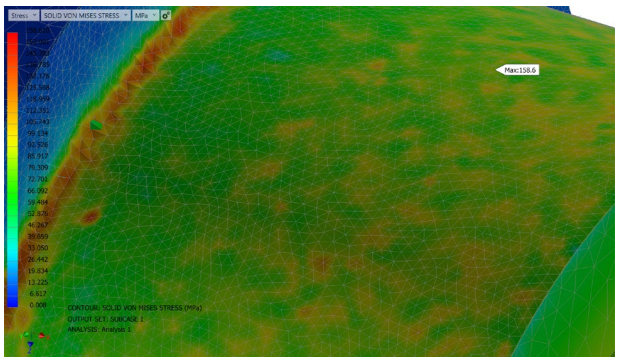

Fig. 5. Test 5 – model discretization, version v01.

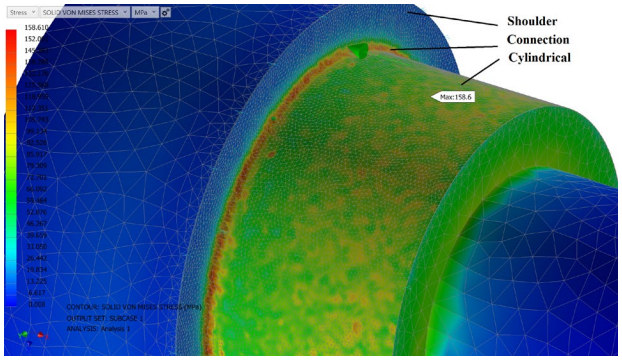

Fig. 6. Test 5 – model discretization, version v02.

For the simulation in question, a reduced model of the shaft (the part containing the bearing on the propeller side) was used. This reduces the number of discretization elements and, consequently, the duration of the simulation (Figs. 5–7). The images highlight the refined discretization in the critical areas.

7. RESULTS AND DISCUSSION: EFFECT OF FILLET RADIUS AND THERMAL SPRAY COATING

After running all of nine tests in Nastran (Inventor Professional), the results (displacement, deformation, von Mises stress and safety factor were analyzed (Table 6). The surfaces of interest are shown in Fig. 6 as *Shoulder*, *Connection* and *Cylindrical*.

7.1. Influence of fillet radius on stress distribution

The finite element analysis confirms that the fillet radius at the shaft shoulder has a dominant influence on the local stress field (maximum Von Mises stress on the connection surface, Fig. 7). Similar trends have been widely reported for stepped shafts and bearing seats, where reduced fillet radii lead to increased stress concentration factors [38] [39] [40]. For the uncoated shaft, decreasing the fillet radius below the maximum value recommended by the bearing manufacturer results in a pronounced increase in the equivalent von Mises

Table 6

Maximum values of the results after running the tests 1-9

Test	Results (max)	Shoulder	Cylindrical	Connection
1	von Mises (MPa)	35	61	143
	Displacement (mm)	0.0006	0.0007	0.0017
	Safety Factor	8	3	4
	Deformed (mm)	0.0006	0.0007	0.0017
2	von Mises (MPa)	51	202	157
	Displacement (mm)	0.0006	0.0018	0.0007
	Safety Factor	0	0	0
	Deformed (mm)	0.0006	0.0017	0.0006
3	von Mises (MPa)	22	185	37
	Displacement (mm)	0.0006	0.0016	0.0006
	Safety Factor	0	0	0
	Deformed (mm)	0.0006	0.0017	0.0006
4	von Mises (MPa)	41	56	131
	Displacement (mm)	0.0005	0.0024	0.0007
	Safety Factor	21	4	3
	Deformed (mm)	0.0005	0.0024	0.0006
5	von Mises (MPa)	56	118	157
	Displacement (mm)	0.0006	0.002132	0.0008
	Safety Factor	8	4	5
	Deformed (mm)	0.0006	0.002132	0.0008
6	von Mises (MPa)	22	150	48
	Displacement (mm)	0.0005	0.0021	0.0006
	Safety Factor	10	0	7
	Deformed (mm)	0.0005	0.002152	0.0006
7	von Mises (MPa)	20	64	106
	Displacement (mm)	0.0007	0.0034	0.0009
	Safety Factor	13	4	4
	Deformed (mm)	0.0007	0.0034	0.0009
8	von Mises (MPa)	46	141	297
	Displacement (mm)	0.0008	0.00277	0.0009
	Safety Factor	8	0	7
	Deformed (mm)	0.0008	0.002776	0.0009
9	von Mises (MPa)	18	109	54
	Displacement (mm)	0.0008	0.0032	0.0011
	Safety Factor	11	4	4
	Deformed (mm)	0.0008	0.0032	0.0011

stress. When the radius is reduced from the nominal value to a sub-optimal value, peak stresses increase by approximately 35–45%, in agreement with classical notch sensitivity studies [39] [41].

Figure 8 shows the displacement after running the test 4 without layer.

Conversely, increasing the fillet radius up to the maximum allowable value leads to a smoother stress distribution and reduced sensitivity to mesh refinement, indicating numerically stable and physically meaningful FEM results [40].

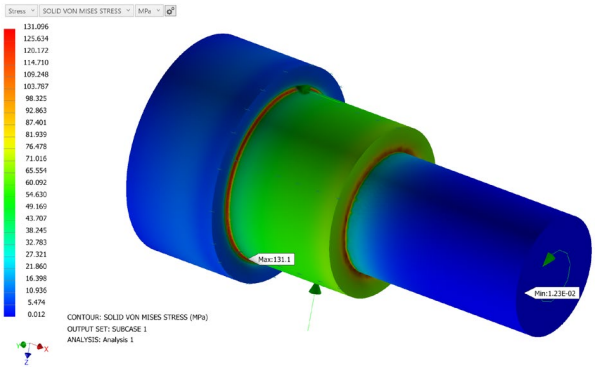

Fig. 7. Test 4 – von Mises Stress (shaft without layer).

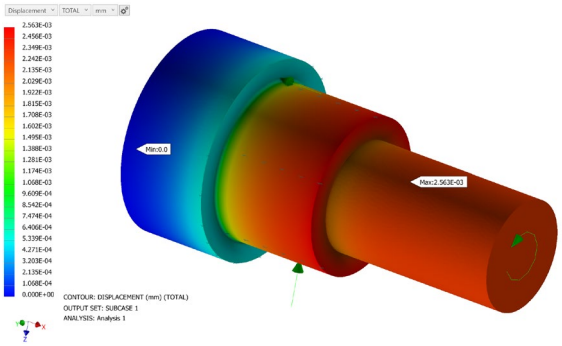

Fig. 8. Test 4 – displacement (shaft without layer).

7.2. Effect of thermal spray coating on the effective fillet geometry

The application of a thermally sprayed coating modifies the effective geometry of the shaft shoulder. For a coating thickness s, the effective fillet radius r_{eff} is reduced from the nominal one r_{nom} according to:

$$r_{eff} = r_{nom} - s. \tag{3}$$

The current research does not take this situation into account for reasons of simplification.

This geometric effect has been previously highlighted in studies addressing repaired or reconditioned shafts, where deposited layers alter local stress raisers even for small thicknesses [42] [43]. Finite element results show that coating thicknesses typical for HVOF and APS processes (200–300 μm) significantly affect the stress field in the fillet region, especially for nominal radii close to the minimum admissible values [43].

7.3. Stress redistribution due to coating–substrate interaction

When the coating layer is explicitly included in the FEM model, the location of maximum stress shifts from the substrate to the coating or to the coating–substrate interface, depending on the elastic properties of the deposited material. This behavior is consistent with previously reported numerical and experimental studies on thermally sprayed coatings subjected to bending and contact loading [7–9] [44] [45] [46].

Rigid cermet coatings such as WC–Co promote stress concentration at the interface due to their high elastic modulus and low compliance mismatch tolerance, while ceramic coatings based on Al_2O_3 (Fig. 9) exhibit elevated stress levels within the coating itself, in line with their limited fracture toughness [45] [47]. Compared to the uncoated shaft, the maximum von Mises stress increases

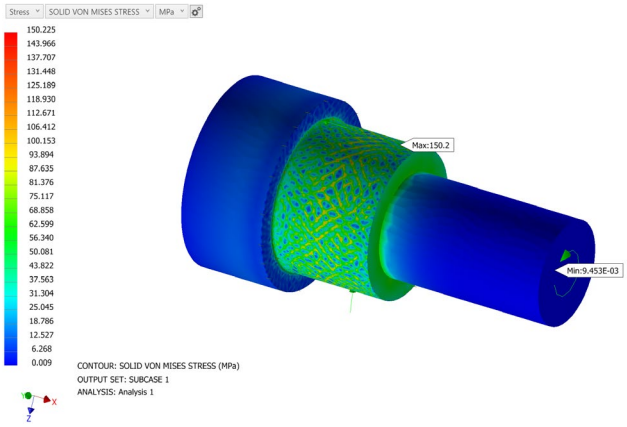

Fig. 9. Test 6 – von Mises Stress (shaft with layer Al2O3 APS).

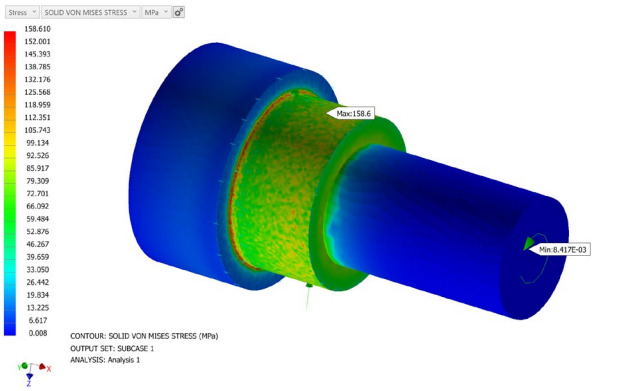

Fig. 10. Test 5 – von Mises Stress (shaft with layer of WC-Co HVOF).

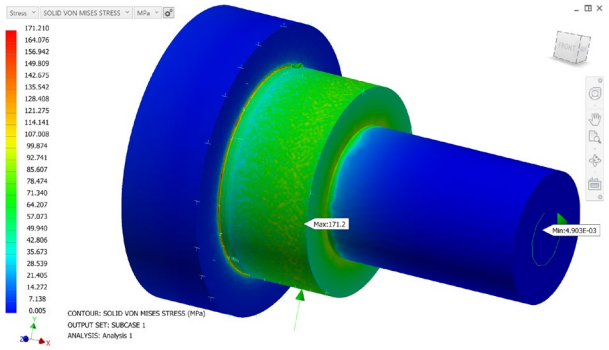

Fig. 11. Test 10 – von Mises Stress (shaft with grinding undercut and layer of WC-Co_HVOF).

by approximately 25–35% for WC–Co (Fig. 10) coatings and up to 60% for ceramic coatings, values comparable to those reported in the literature for coated steel substrates [46] [47].

Figure 11 depicts the behavior of the shaft (von Mises Stress) with grinding undercut and layer of WC-Co HVOF under loads.

7.4. Combined effect of fillet radius and coating thickness

The FEM results highlight a synergistic effect between fillet radius and coating thickness. Shafts designed with fillet radii close to the lower admissible limit become particularly sensitive to the presence of a coating layer. Similar observations were reported by Pawlowski and subsequent authors, who emphasized that geometric stress raisers dominate the mechanical response of coated components under cyclic loading [42] [43] [44].

In contrast, shafts designed with fillet radii near the upper allowable limit maintain acceptable stress levels after coating application, confirming that proper geometric design can partially compensate for stiffness mismatch and coating-induced stress amplification 43] 46].

The shaft model with grinding undercut (d = 35 mm, r_a = 0.1 mm, h = 0.2 mm, l = 1.8 mm) and deposited layer (Figs. 2 and 12), loaded similarly to the other models (T = 130 N, Q = 7 Nm, P_{ax} = 1.7 MPa, $P_{cyl\ max}$ = 60 MPa.), was also numerically simulated. It is found that the von Mises equivalent stresses (max. 171 MPa, Table 7, Fig. 13), as well as the deformations (max. 2.7 µm, Fig. 14), follow the same trend in the undercut area as for the previous tests.

Table 7

Maximum values of the results after running the test 10

Test	Results (max)	Shoulder	Cylindrical	Undercut
10 without layer	von Mises (MPa)	13	57	118
	Displacement (mm)	0.0002	0.0029	0.0004
	Safety Factor	18	4	5
	Deformed (mm)	0.0002	0.0027	0.0004
10 layer - WC-Co_HVOF	von Mises (Mpa)	36	105	171
	Displacement (mm)	0.0003	0.0026	0.0006
	Safety Factor	10	5	7
	Deformed (mm)	0.0003	0.0026	0.0006

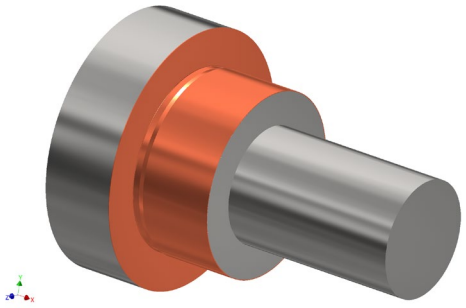

Fig. 12. Shaft model with grinding undercut and layer.

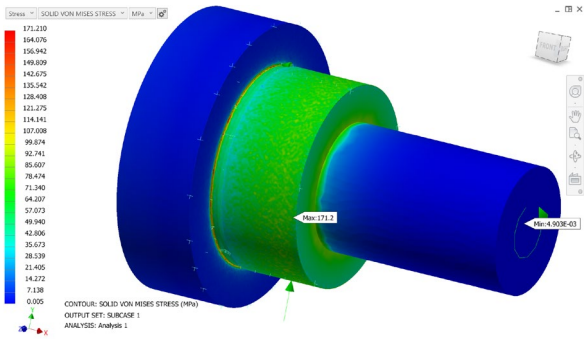

Fig. 13. Test – von Mises Stress (shaft with undercut and layer of WC-Co_HVOF).

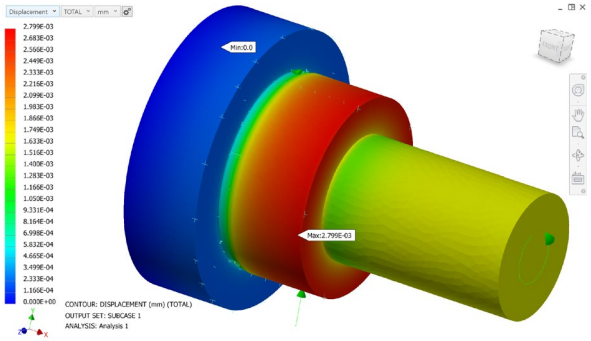

Fig. 14. Test – deformation (shaft with undercut and layer of WC-Co_HVOF).

Table 8

Trends of the von Mises Stress influence

Factor	Shoulder	Cylindrical	Connection
d	↓ slight	none	↑ small
r_s	↓ strong	↑ moderate	↑ strong
s	none	↑ large	↑ large

7.5. Implications for structural integrity and bearing compatibility

Although larger fillet radii generally reduce stress concentration in the shaft, exceeding the maximum radius permitted by the bearing chamfer leads to incomplete axial contact between the bearing ring and the shaft shoulder. This phenomenon has been documented in bearing design standards and manufacturer guidelines, which emphasize strict compliance with chamfer and fillet compatibility [48], ISO 15:2017.

FEM results corresponding to oversized fillet radii may therefore underestimate stresses in the shaft while introducing non-physical boundary conditions at the bearing interface, potentially leading to premature bearing failure despite favorable numerical stress values [48].

7.6. Design recommendation based on fem results

Even though the statistical model is based on only 9 tests, the data suggests some practical trends (Table 8):

- r_s appears to be the most influential parameter, strongly affecting all outputs (especially Connection and Cylindrical).
- s shows a positive effect on *Cylindrical* and *Connection*, but results are inconsistent.
- d has a minor influence, with only small changes across outputs.

From an engineering perspective, adjusting the fillet radius r_s is likely the most effective way to control the results, while the diameter d plays a secondary role.

Based on the numerical results and consistent with prior studies on coated mechanical components [42] [43] [44], the fillet radius for reconditioned shafts should be selected by explicitly accounting for the coating thickness:

$$r_{nom} \geq r_{s\,\max} + s. \tag{6}$$

This condition ensures that the effective fillet radius after coating remains within the admissible range for the bearing while minimizing stress concentration effects. Neglecting the interaction between fillet geometry and thermal spray coatings can therefore lead to non-conservative assessments of structural integrity, as also reported in recent FEM-based investigations of repaired shafts [43] [46].

8. FUTURE WORK

Future work will extend the current numerical investigation by developing the stress distributions and parametric results obtained in this study.

First, the inclusion of residual stresses induced by the thermal spraying process will be addressed. In the current analysis, the coating layer was assumed to be free of initial stresses. However, the stress concentrations observed at the coating–substrate interface and in the bearing shoulder region suggest that spray-induced residual stresses may influence significantly the overall stress state. Future models will incorporate thermo-mechanical simulations of the spraying process or experimentally measured residual stress profiles to evaluate their interaction with service loads.

In addition, fatigue life evaluation can be investigated as an extension of the static stress analysis presented in this paper. The high equivalent stress levels identified in the shoulder fillet region indicate potential fatigue-critical zones under cyclic loading. The finite element stress results will be coupled with fatigue damage models to estimate the service life of reconditioned wells under load spectrum conditions representative of UAVs.

Next, advanced modeling of the coating-substrate interface will be considered, drawing on research addressing this aspect [49] [50] [51]. In the present model, perfect bonding was assumed at the interface; however, the stress gradients observed across the coating thickness highlight the importance of interfacial behavior. Cohesive zone models or damage-based interface models will be used to investigate the onset and progression of delamination under mechanical loading.

Additionally, parametric optimization of the reconditioning layer will be pursued. The influence of coating thickness on stress distribution demonstrates that geometric and material parameters strongly affect structural integrity. The finite element model will integrate with design of experiments or optimization techniques to identify parameter combinations that minimize stress concentrations while maintaining functional requirements.

Last but not least, one can also investigate the aspect related to experimental validation and multi-scale modeling for supporting the numerical findings. The stress trends and critical regions identified in the FEM results will guide experimental testing and microstructural analysis. Incorporating coating microstructural features, such as porosity and splat morphology, into future numerical models may further improve the predictive capability [52] of structural integrity assessments for thermally sprayed components.

8. CONCLUSIONS

The present study highlights the critical role of geometric and material parameters in the structural performance of UAV shafts reconditioned thermal spray coatings. Among the investigated factors, the fillet radius was identified as the dominant parameter influencing stress concentration, with smaller radii leading to significantly higher stress levels in critical regions. The introduction of thermal spray coatings was shown to modify the stress distribution, generating additional stress concentrations, particularly at the coating–substrate interface.

Furthermore, coating material properties were found to govern stress localization, with high-stiffness coatings shifting stresses toward the interface, while lower-stiffness coatings exhibited increased stress within the coating layer. Coating thickness also plays a significant role, as increased thickness can amplify stress gradients if not properly optimized.

Although the statistical analysis was limited by the reduced number of simulation cases, consistent trends were observed, providing valuable qualitative insights. Overall, the results emphasize the need for careful optimization of fillet geometry and coating characteristics to ensure structural integrity and reliability of reconditioned shafts.

REFERENCES

[1] *Journal of Thermal Spray Technology*, Online]. Available: https://link.springer.com/journal/11666

[2] A. G. M. Pukasiewicz, H. E. de Boer, G. B. Sucharski, R. F. Vaz, and L. A. J. Procopiak, ‘The influence of HVOF spraying parameters on the microstructure, residual stress and cavitation resistance of FeMnCrSi coatings’, *SURFACE & COATINGS TECHNOLOGY*, vol. 327, pp. 158–166, Oct. 2017, doi: 10.1016/j.surfcoat.2017.07.073.

[3] J. Pina, A. Dias, and J. Lebrun, ‘Study by X-ray diffraction and mechanical analysis of the residual stress generation during thermal spraying’, *MATERIALS SCIENCE AND ENGINEERING A-STRUCTURAL MATERIALS PROPERTIES MICROSTRUCTURE AND PROCESSING*, vol. 347, no. 1–2, pp. 21–31, Apr. 2003, doi: 10.1016/S0921-5093(02)00580-4.

[4] P. Bansal, P. H. Shipway, and S. B. Leen, ‘Residual stresses in high-velocity oxy-fuel thermally sprayed coatings - Modelling the effect of particle velocity and temperature during the spraying process’, *ACTA MATERIALIA*, vol. 55, no. 15, pp. 5089–5101, Sep. 2007, doi: 10.1016/j.actamat.2007.05.031.

[5] R. Ghafouri-Azar, J. Mostaghimi, and S. Chandra, ‘Modeling development of residual stresses in thermal spray coatings’, *COMPUTATIONAL MATERIALS SCIENCE*, vol. 35, no. 1, pp. 13–26, Jan. 2006, doi: 10.1016/j.commatsci.2005.02.007.

[6] A. M. Kamara and K. Davey, ‘A numerical and experimental investigation into residual stress in thermally sprayed coatings’, *INTERNATIONAL JOURNAL OF SOLIDS AND STRUCTURES*, vol. 44, no. 25–26, pp. 8532–8555, Dec. 2007, doi: 10.1016/j.ijsolstr.2007.06.031.

[7] J. Martinez-Garcia, V. Martinez-Garcia, and A. Killinger, ‘Multi-Scale Thermo-Mechanical Model Simulation of Residual Stress in Atmospheric Plasma Spray Process’, *COATINGS*, vol. 14, no. 12, Dec. 2024, doi: 10.3390/coatings14121547.

[8] M. Hauer, S. Krebs, W. Kroemmer, and K.-M. Henkel, ‘Correlation of Residual Stresses and Coating Properties in Arc-Sprayed Coatings on Different Substrates for Maritime Applications’, *JOURNAL OF THERMAL SPRAY TECHNOLOGY*, vol. 29, no. 6, pp. 1289–1299, Aug. 2020, doi: 10.1007/s11666-020-01020-x.

[9] W. Luo, U. Selvadurai, and W. Tillmann, ‘Effect of Residual Stress on the Wear Resistance of Thermal Spray Coatings’, *JOURNAL OF THERMAL SPRAY TECHNOLOGY*, vol. 25, no. 1–2, pp. 321–330, Jan. 2016, doi: 10.1007/s11666-015-0309-0.

[10] C. M. Roper, C. M. Fancher, J. R. Bunn, and L. N. Brewer, ‘Residual Stress in Cold Spray SS304L Measured Via Neutron Diffraction and Comparison of Analytical Models to Predict the Residual Stress’, *JOURNAL OF MATERIALS ENGINEERING AND PERFORMANCE*, vol. 33, no. 15, SI, pp. 7626–7637, Aug. 2024, doi: 10.1007/s11665-024-09422-6.

[11] H. Ng and Z. Gan, ‘A finite element analysis technique for predicting as-sprayed residual stresses generated by the plasma spray coating process’, *FINITE ELEMENTS IN ANALYSIS AND DESIGN*, vol. 41, no. 13, pp. 1235–1254, Jul. 2005, doi: 10.1016/j.finel.2005.02.002.

[12] V. Singh, A. Bansal, and A. K. Singla, ‘Optimization of High-Velocity Oxygen Fuel Spray Process Parameters to Achieve Maximum Thickness and Minimum Porosity in Vanadium Carbide Coating’, *JOURNAL OF MATERIALS ENGINEERING AND PERFORMANCE*, vol. 33, no. 24, pp. 14256–14265, Dec. 2024, doi: 10.1007/s11665-023-08964-5.

[13] J. Wang, P. Hodgson, J. Zhang, and C. Yang, ‘Residual thermal stresses in a Fe3Al/Al2O3 gradient coating system’, in *FRONTIERS IN MATERIALS SCIENCE AND TECHNOLOGY*, J. Bell, C. Yan, L. Ye, and L. Zhang, Eds, in Advanced Materials Research, vol. 32. 2008, p. 71+. doi: 10.4028/www.scientific.net/AMR.32.71.

[14] T. Varis, T. Suhonen, J. Laakso, M. Jokipii, and P. Vuoristo, ‘Evaluation of Residual Stresses and Their Influence on Cavitation Erosion Resistance of High Kinetic HVOF and HVAF-Sprayed WC-CoCr Coatings’, *JOURNAL OF THERMAL SPRAY TECHNOLOGY*, vol. 29, no. 6, pp. 1365–1381, Aug. 2020, doi: 10.1007/s11666-020-01037-2.

[15] F. Oviedo and A. Valarezo, ‘Residual Stress in High-Velocity Impact Coatings: Parametric Finite Element Analysis Approach’, *JOURNAL OF THERMAL SPRAY TECHNOLOGY*, vol. 29, no. 6, pp. 1268–1288, Aug. 2020, doi: 10.1007/s11666-020-01026-5.

[16] F. Torres and R. Fernandez, ‘Effect of Thickness on the Residual Stress Profile of an Aluminum Cold Spray Coating by Finite Element Analysis’, *COATINGS*, vol. 14, no. 6, Jun. 2024, doi: 10.3390/coatings14060665.

[17] J. Martínez-García, V. Martínez-García, and A. Killinger, 'Multi-Scale Modeling of Residual Stress in Atmospheric Plasma Spray Process', *Coatings*, vol. 14, no. 12, p. 1547, 2024, doi: 10.3390/coatings14121547.

[18] S. Sayahlatifi and others, '3D Microstructure-Based Finite Element Simulation of Cold-Sprayed Al–Al2O3 Composite Coatings Under Quasi-Static Compression', *Journal of Thermal Spray Technology*, vol. 31, pp. 102–118, 2021, doi: 10.1007/s11666-021-01260-5.

[19] N. Nayebpashaee, S. Seyedein, M. Aboutalebi, H. Sarpoolaky, and S. Hadavi, 'Finite element simulation of residual stress and failure mechanism in plasma sprayed thermal barrier coatings using actual microstructure as the representative volume', *Surface and Coatings Technology*, vol. 291, pp. 103–114, 2016.

[20] A. R. Silva, J. R. A. Martins, and P. Paglione, 'Electric Propulsion Systems for Small UAVs: A Review', *Energies*, vol. 15, no. 2, p. 455, 2022, doi: 10.3390/en15020455.

[21] J. G. Leishman, *Principles of Helicopter Aerodynamics*. Cambridge University Press, 2006.

[22] M. Hassanalian and A. Abdelkefi, 'Classifications, Applications, and Design Challenges of Drones: A Review', *Progress in Aerospace Sciences*, vol. 91, pp. 99–131, 2017, doi: 10.1016/j.paerosci.2017.04.003.

[23] L. Markovska, K. Balalaieva, and A. Balalaiev, 'Assessment of Thrust Force of UAV Propellers', *Aerospace Technic and Technology*, pp. 28–35, 2021.

[24] T. Madani and A. Benallegue, 'Backstepping control for a quadrotor helicopter', in *2006 IEEE/RSJ International Conference on Intelligent Robots and Systems*, IEEE, 2006, pp. 3255–3260.

[25] A. A. Abubakar, A. F. M. Arif, K. S. Al-Athel, S. S. Akhtar, and J. Mostaghimi, 'Modeling Residual Stress Development in Thermal Spray Coatings: Current Status and Way Forward', *J Therm Spray Tech*, vol. 26, no. 6, pp. 1115–1145, Aug. 2017, doi: 10.1007/s11666-017-0590-1.

[26] M. Drela, *QPROP Formulation*. 2006. Online]. Available: https://web.mit.edu/drela/Public/web/qprop/qprop_theory.pdf

[27] X. Liu, D. Zhao, and N. L. Oo, 'Comparison studies on aerodynamic performances of a rotating propeller for small-size UAVs', *Aerospace Science and Technology*, vol. 133, p. 108148, 2023.

28] M. Zhang, J. Jiao, J. Zhang, and others, 'Aerodynamic Performance Modeling Method of High-Altitude Propellers Across the Entire Flight Envelope', *Scientific Reports*, vol. 15, p. 11296, 2025, doi: 10.1038/s41598-025-95445-5.

[29] Y. Han, Z. Liu, and W. Zhang, 'Aeroelastic Response of UAV Propellers in Forward Flight', *Aerospace Science and Technology*, vol. 128, p. 107673, 2024, doi: Han.

[30] E. Pegane-Vingadas and others, 'Effect of Laser Texturing in Thermal Spraying on the Fatigue Life of the Ti-6Al-4V Alloy', *Journal of Thermal Spray Technology*, vol. 34, pp. 714–734, 2025, doi: 10.1007/s11666-024-01912-2.

[31] M. Ksiazek, I. Nejman, and L. Boron, 'Investigation on microstructure, mechanical and wear properties of hvof sprayed composite coatings (Wc–Co+ Cr) on ductile cast iron', *Materials*, vol. 14, no. 12, p. 3282, 2021.

[32] M. Nowakowska, L. Łatka, P. Sokołowski, M. Szala, F.-L. Toma, and M. Walczak, 'Investigation into microstructure and mechanical properties effects on sliding wear and cavitation erosion of Al2O3–TiO2 coatings sprayed by APS, SPS and S-HVOF', *Wear*, vol. 508, p. 204462, 2022.

[33] L. Pawlowski, *The science and engineering of thermal spray coatings*. John Wiley & Sons, 2008.

[34] O. Ali *et al.*, 'Influence of feedstock and thermal spray process on the phase composition of alumina coatings and their sliding wear', *Journal of thermal spray technology*, vol. 32, no. 7, pp. 2028–2053, 2023.

[35] A. Garfias Bulnes, V. Albaladejo Fuentes, I. Garcia Cano, and S. Dosta, 'Understanding the Influence of High Velocity Thermal Spray Techniques on the Properties of Different Anti-Wear WC-Based Coatings', *Coatings*, vol. 10, no. 12, 2020, doi: 10.3390/coatings10121157.

[36] 'NTN catalog. Shaft and Housing Design'. NTN. Online]. Available: https://www.ntnglobal.com/en/products/catalog/pdf/2203E_a14.pdf

[37] 'Shaft and Housing Design'. NTM. Online]. Available: https://www.ntnglobal.com/en/products/catalog/pdf/2203E_a14.pdf

[38] R. E. Peterson, *Stress Concentration Factors*. New York: John Wiley & Sons, 1974.

[39] W. D. Pilkey and D. F. Pilkey, *Peterson's Stress Concentration Factors*, 3rd edn. John Wiley & Sons, 2008.

[40] R. L. Norton, *Machine Design: An Integrated Approach*, 6th edn. Pearson, 2019.

[41] D. Gross and T. Seelig, *Fracture Mechanics: With an Introduction to Micromechanics*, 3rd edn. Springer, 2018. doi: 10.1007/978-3-319-71001-3.

[42] L. Pawlowski, *The Science and Engineering of Thermal Spray Coatings*. John Wiley & Sons, 2008.

[43] M. Nowakowska, L. Łatka, M. Michalak, and others, 'Investigation into microstructure and mechanical properties of Al_2O_3–TiO_2 coatings sprayed by APS, SPS and S-HVOF', *Wear*, vol. 508–509, p. 204462, 2022, doi: 10.1016/j.wear.2022.204462.

[44] R. S. Lima and B. R. Marple, 'Thermal spray coatings engineered from nanostructured ceramic agglomerated powders', *Surface and Coatings Technology*, vol. 202, no. 7, pp. 1465–1474, 2007, doi: 10.1016/j.surfcoat.2007.06.019.

[45] M. Książek, Ł. Boron, and others, 'Mechanical behavior of HVOF-sprayed WC–Co coatings', *Materials*, vol. 14, no. 12, p. 3282, 2021, doi: 10.3390/ma14123282.

[46] R. Ahmed, M. Hadfield, and others, 'Finite element analysis of stress distribution in thermally sprayed coated steel components', *Surface and Coatings*

Technology, vol. 357, pp. 1015–1026, 2019, doi: 10.1016/j.surfcoat.2018.10.086.

[47] L. Pawlowski and P. Fauchais, 'Residual stresses and mechanical behavior of thermal spray coatings', *Journal of Thermal Spray Technology*, vol. 16, no. 4, pp. 475–486, 2007, doi:10.1007/s11666-007-9067-3.

[48] *Rolling Bearings Catalogue*. Gothenburg, Sweden: SKF Group, 2022.

[49] S. M. Bostancı, 'Finite Element Modelling of Thermal Barrier Coating Failure Mechanisms Using XFEM and Cohesive Zone Method', PhD Thesis, Middle East Technical University, 2019. Online]. Available: https://open.metu.edu.tr/handle/11511/45328

[50] S. Sfarra et al., 'Cohesive Zone Modelling of Thermal Barrier Coatings Interfacial Properties Based on Three-Dimensional Observations and Mechanical Testing', *Surface and Coatings Technology*, vol. 237, pp. 95–104, 2013, doi: 10.1016/j.surfcoat.2013.09.065.

[51] A. Sapora and M. Paggi, 'A coupled cohesive zone model for transient analysis of thermoelastic interface debonding', *Computational Mechanics*, vol. 53, no. 4, pp. 845–857, Oct. 2013, doi: 10.1007/s00466-013-0934-8.

[52] W. Rannetbauer, S. Hubmer, C. Hambrock, and R. Ramlau, 'Predictive Modelling of Critical Variables for Improving HVOF Coating Using Gamma Regression Models', *arXiv preprint*, 2023.